applied sciences

MDPI

Article

Effect of the Geometric Configuration of the Disc Cutter on the Cutting Behaviour in Tunneling

Yixin Duan [1,2], Dajun Yuan [1,2,*], Jun Wu [3], Xiaojie Deng [4], Bing Wu [5] and Zhangang Sun [4]

[1] Key Laboratory of Urban Underground Engineering, Ministry of Education, Beijing Jiaotong University, Beijing 100044, China
[2] School of Civil Engineering, Beijing Jiaotong University, Beijing 100044, China
[3] China State Construction Engineering Corporation, Beijing 100029, China
[4] Jinan Rail Transit Group Co., Ltd., Jinan 250101, China
[5] China Railway No. 2 Engineering Group Co., Ltd., Chengdu 610031, China
* Correspondence: djyuan@bjtu.edu.cn

Abstract: The disc cutter is a key tool in shield machines that come into direct contact with rock while participating in the removal of rock. Therefore, the reasonable design of the geometric configuration of disc cutters greatly determines the tunnelling efficiency of the shield machine. In this paper, the factors influencing the rock-breaking behaviour of disc cutters are studied. Firstly, to ensure the accuracy of the rock-breaking simulation, the parameters of the Holmquist–Johnson–Cook model of the diorite in the Jinan area were determined. Secondly, using ANSYS/LS-DYNA to simulate the rock-breaking process, the influence of the geometric configuration, including blade width and blade fillet, on rock-breaking behaviour was analysed. The results show that with increasing depth of penetration, the contact force increases approximately linearly. The contact force and the rock-breaking influence range gradually decrease with increasing number of blade fillets. In addition, with increasing number of blade fillets, the shape of the influence range gradually transitions from an approximate circle to a trapezoid, and finally to a triangle. With increasing blade width, the contact force and the rock-breaking influence range both increase, but the shape of the influence range remains largely unchanged as a trapezoid. On the basis of these research results, this paper gives some suggestions for the selection and configuration of disc cutters in different strata, which can give some guidance for practical engineering.

Keywords: shield tunnel; disc cutter; rock-breaking; HJC model; numerical simulation; cutter geometric configuration

check for updates

Citation: Duan, Y.; Yuan, D.; Wu, J.; Deng, X.; Wu, B.; Sun, Z. Effect of the Geometric Configuration of the Disc Cutter on the Cutting Behaviour in Tunneling. *Appl. Sci.* **2023**, *13*, 72. https://doi.org/10.3390/app13010072

Academic Editors: Peng Zhang, Xuefeng Yan, Cong Zeng and Fang Xu

Received: 21 October 2022
Revised: 9 December 2022
Accepted: 19 December 2022
Published: 21 December 2022

Copyright: © 2022 by the authors. Licensee MDPI, Basel, Switzerland. This article is an open access article distributed under the terms and conditions of the Creative Commons Attribution (CC BY) license (https://creativecommons.org/licenses/by/4.0/).

1. Introduction

With the advances in infrastructure construction in China, the number of tunnels constructed is increasing year by year [1–5]. The shield method has gradually become the mainstream method of tunnel construction, due to advantages which include a high degree of mechanization, high construction efficiency, and the possibility of performing construction with water, and it is widely used for the construction of highways, railways, electric power, urban rail transit, etc. [6–8]. Disc cutters, as a direct tool used by the shield machine to break up rock and soil, has a crucial impact on the efficiency and safety of the construction of the shield tunnel. The use of an appropriate design for the disc cutter is extremely important in the construction of shield tunnels. There are many factors affecting the rock-breaking efficiency of disc cutters, including the size of the disc cutter, blade width, blade angle, blade fillet, the properties of the rock and soil, etc. [9]. Therefore, to improve the rock-breaking efficiency of the disc cutter, it is necessary to optimize the design according to the factors influencing the rock breaking.

Many researchers have studied rock properties and the performance of disc cutters in recent years. In the numerical simulation of rock breaking with disc cutters, the most

commonly used rock dynamic computational constitutive model is the HJC (Holmquist–Johnson–Cook) model [10–12]. The HJC model was originally a constitutive model for simulating concrete taking into consideration the strain rate effects, damage effects, confining pressure effects, crushing effects and compaction effects when subjected to large strains, high strain rates, and high pressure [13,14]. Since the crushing process of rock is highly consistent with that of concrete, it can also be used to simulate the breaking behaviour of rock. In recent years, many scholars have studied methods for determining the HJC model parameters. Based on the concrete strength calculation formula proposed by the American Concrete Association, Zhang and Li [15] gave a simple method for deriving other basic mechanical parameters in the HJC model from the uniaxial compressive strength, but the limitation of this method is that it does not include the limit surface parameters of the HJC model. Polanco-Loria et al. [16,17] enhanced the pressure-shear behaviour of the HJC model and changed the modelling of strain rate sensitivity so that the enhancement factor of strain rate goes to unity for a strain rate of zero. Based on the yield surface theory, Xiong et al. [18,19] established the relationship between the cohesion strength and the parameters of the Mohr–Coulomb criterion and proposed a method for obtaining the limit surface parameters of the HJC model. Zhang et al. [20] proposed a method for determining the failure strength parameters and obtained the value of the failure strength parameters. Fang et al. [21] derived the relationship between the cohesion parameter and the cap model parameters based on the plastic yield surface theory. Sun et al. [22] analysed the failure type parameter in the parameters of the HJC model, studied the influence of this parameter on concrete compaction failure, and determined its value range. Su et al. [23] investigated the previous studies and was able to obtain the strength parameters, state parameters, rate effect parameters, and damage parameters of the HJC model through the analysis and fitting of existing experimental data. In addition, the relevant parameters were revised according to the results of the shield cutting tool cutting concrete test. Since the HJC model was originally used to describe the failure behaviour of concrete, most of the initial parameters are not suitable for rock materials. Therefore, to accurately describe the failure behaviour of rocks, scholars have carried out many studies regarding the determination of the parameters of the HJC model for rocks. At present, a series of HJC model parameters of rocks or rock-like media have been determined, including limestone, granite porphyry, granite, sandstone, marble, and coal [24–28].

Scholars have performed research analysing the structural design and rock-breaking efficiency, and simulating the rock-breaking process of shield disc cutters. Regarding the structural design of disc cutters, Frenzel et al. [29] found that changes in blade width had less effect on disc cutter wear. Zhao et al. [30] designed a parametric model of the variable cross-section (VCS) cutter ring and used FEM to simulate rolling behaviour, and the results showed that the VCS cutter ring applied a periodic force to the rocks during the rolling process. With regard to rock-breaking efficiency, Teale [31] proposed the concept of specific energy, which is defined as the energy required to excavate a unit volume of rock. Gertsch et al. [32] found that the spacing between disc cutters had a greater impact on specific energy than penetration, and a spacing of 76 mm was close to optimum in hard and brittle crystalline rock. Ning et al. [33] carried out a full-scale cutting test for a 432 mm disc cutter with three different blade widths, and found that the specific energy and optimal spacing were positively related to blade width. Scholars have also performed a lot of work on the numerical simulation of rock-breaking using shield disc cutters. Cho et al. [34] used AUTODYN-3D to simulate the three-dimensional dynamic failure observed in LCM tests and determined the optimum cutter spacing by calculating the specific energy. Li et al. [35] built a model of a disc cutter by Pro/E and carried out a numerical simulation of rock-breaking using the disc cutter. The results showed that the disc cutter was able to cut hard rock, and the contact force was in agreement with the common prediction formula for disc cutter forces, which showed that the modelling method was correct and feasible. Zhang et al. [36] established five rock-breaking models for disc cutters with different diameters and penetrations, and found that with increasing disc cutter diameter and penetration,

the contact force increased as well. Choi et al. [37] implemented a numerical simulation of the optimum cutter spacing and failure aspects of Korean tuff, and the results were compared with those of the LCM test, showing that the numerical method was correct. Labra et al. [38] created a numerical model that combined the advantages of DEM and FEM to more accurately simulate the rock-breaking process of a disc cutter. Zhou et al. [39] developed a general particle dynamics code to simulate the rock-breaking process of a disc cutter in the mixed-face ground, and a novel algorithm of the contacts at the boundary between the two different media was proposed.

By investigating existing studies, it can be found that the existing research on the structural design and numerical simulation of disc cutters is not specific enough, and only describes the general influence of geometric configuration on the rock-breaking behaviour of the disc cutter, without further considering the influence of geometric configuration.

This paper aims to explore the influence of the geometric configuration of the disc cutter on the rock-breaking process and to provide guidance for the design and selection of the geometric configuration of the disc cutter. Section 1 introduces the currently existing research and provides a brief introduction to the work carried out in this paper. In Section 2, a comprehensive introduction to the HJC model is provided, including the strength equation, state equation, and damage equation. To ensure the accuracy of the numerical simulation, Section 3 introduces a method for determining the parameters of the diorite HJC model in the Jinan area, and uses the uniaxial compression test, triaxial compression test, Brazilian splitting test and split Hopkinson compression bar test to determine the parameters of the HJC model in the Jinan area. Section 4 describes the numerical simulation of the rock-breaking process of the disc cutter, including the establishment of the model and the results of the simulation, and identifies the geometric configuration that influences the rock-breaking behaviour, including aspects such as blade width and blade fillet, and reveals the influence of geometric configuration of the disc cutter on the rock-breaking process, including rock-breaking force and the impact range. Section 5 summarizes the conclusions of this study.

2. An Overview of the HJC Model

The HJC (Holmquist–Johnson–Cook) constitutive model comprehensively considers the effects of high strain, high strain rate, and high pressure. This model is divided into three parts: the strength equation, the damage equation and the state equation.

2.1. Strength Equation

The strength equation in the HJC model is shown in Figure 1, and its strength function is as follows:

$$\sigma^* = [A(1-D) + BP^{*N}][1 + \mathrm{CIn}\,\dot{\varepsilon}^*] \quad (1)$$

The normalized dimensionless equivalent stress is expressed as a function of damage, pressure and strain rate. In this equation, σ^* is defined as $\sigma^* = \sigma/f_c'$ (σ is the actual equivalent stress, f_c' is quasi-static uniaxial compressive strength); P^* is defined as $P^* = P/f_c'$ (P is actual pressure); $\dot{\varepsilon}^*$ defined as $\dot{\varepsilon}^* = \dot{\varepsilon}/\varepsilon_0$ ($\dot{\varepsilon}$ is actual strain rate, ε_0 is reference strain rate, $\varepsilon_0 = 1.0\ \mathrm{s}^{-1}$); A is the normalized cohesive strength; B is the normalized pressure hardening coefficient; C is the strain rate coefficient; and N is the pressure hardening exponent. Since σ^* increases as P^* increases, there is a limit value for σ^*, defined as $S_{\max}$, which is the normalized maximum intensity.

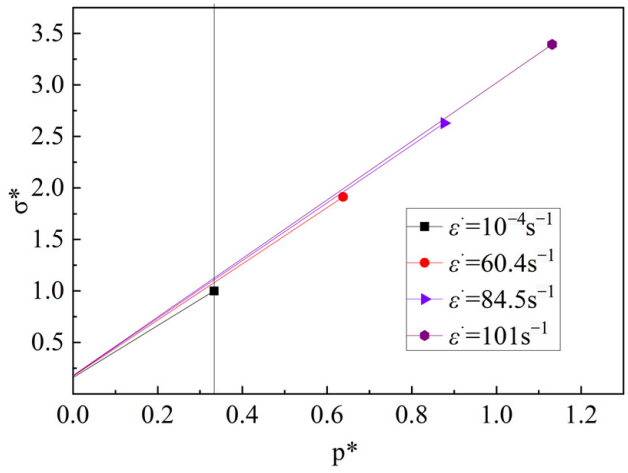


Figure 1. Technique for removing the pressure effect.

2.2. Damage Equation

The damage equation in the HJC model is shown in Figure 2; its damage function is as follows, where D is the damage factor ($0 \le D \le 1$):

$$D = \sum \frac{\Delta\varepsilon_p + \Delta\mu_p}{D_1(P^* + T*)^{D_2}} \tag{2}$$

$$\varepsilon_p^f + \varepsilon_p^f = D_1(P^* + T^*)^{D_2} \ge EF \min \tag{3}$$

In this equation, $\Delta\varepsilon_p$ and $\Delta\mu_p$ are the equivalent plastic strain increment and plastic volumetric strain increment, respectively; $D_1(P^* + T^*)^{D2}$ is the fracture plastic strain under a constant pressure P, where D_1 and D_2 are both constants; $T^* = T/f_c^{'}$, T is maximum tensile hydrostatic strength. Since the rock material cannot bear any plastic strain when $P^* = -T^*$, and the damage factor increases with increasing P^*, the third damage constant, namely the minimum damage constant ε_{fmin}, is added; *EFmin* is the minimum plastic strain when the material is fractured, which is used to control the brittle cracking of the material caused by the tensile stress.

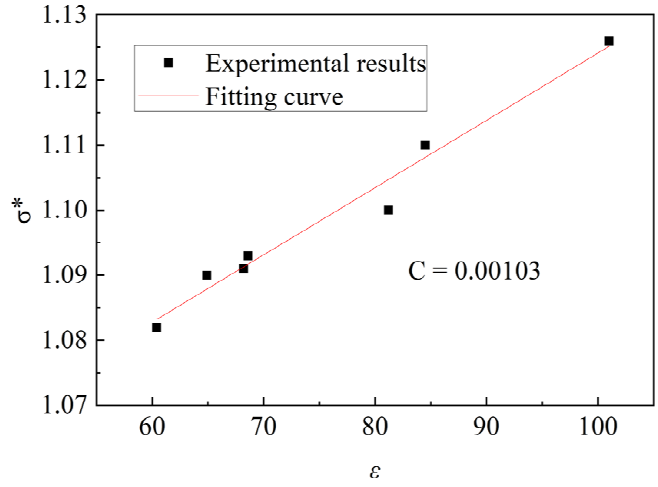


Figure 2. Determination of the strain rate constant.

2.3. State Equation

The state equation in the HJC model can be divided into three regions: the linear elastic region, the transition region, and the fully dense region.

(1) Linear elastic region ($0 \le \mu \le \mu_{crush}$)

The pressure in the linear elastic region is expressed as follows:

$$P = K_{elastic}\mu \tag{4}$$

In this equation, P is pressure; μ is volumetric strain, $\mu = (\rho/\rho_0) - 1$; ρ and ρ_0 are the current density and initial density, respectively; $K_{elastic}$ is the elastic bulk modulus, $K_{elastic} = P_{crush}/\mu_{crush}$, P_{crush} and μ_{crush} are pressure and volumetric strain under the elastic compression limit.

(2) Transition region ($\mu_{crush} < \mu \leq \mu_{lock}$)

In this region, the air is gradually compressed out of the holes of the rock material, and there will be a plastic volumetric strain in the rock material. At this time, the pressure of the material during loading and unloading is expressed as follows:

$$P = P_{crush} + \frac{P_{lock} - P_{crush}}{\mu_{lock} - \mu_{crush}} \tag{5}$$

$$P = P_{crush} + \frac{P_{lock} - P_{crush}}{\mu_{lock} - \mu_{crush}}(\mu_0 - \mu_{crush}) + [(1 - F)K_{elastic} + F\frac{P_{lock} - P_{crush}}{\mu_{lock} - \mu_{crush}}](\mu - \mu_0) \tag{6}$$

In this equation, μ_{lock} and P_{lock} are volumetric strain and pressure, respectively, in the transition region; F is the unloading coefficient, which is expressed as follows:

$$F = (\mu_0 - \mu_{crush})/(\mu_{lock} - \mu_{crush}) \tag{7}$$

(3) Fully dense region ($\mu_{lock} < \mu$)

In this region, the air is fully removed from the rock mass. At this time, the pressure of the material during loading and unloading is expressed as follows:

$$P = K_1\overline{\mu} + K_2\overline{\mu}^2 + K_3\overline{\mu}^3 \tag{8}$$

$$P = K_1\overline{\mu} \tag{9}$$

In this equation, $\overline{\mu} = \frac{\mu - \mu_{lock}}{1 + \mu_{lock}}$ is the modified volumetric strain; μ_{lock} is the volumetric strain of the rock material compaction point; and K_1, K_2 and K_3 are rock material constants.

3. Determination of HJC Model Parameters of Diorite in the Jinan Region

The diorite specimen used in this paper was taken from a shield tunnel project on Jinan metro line 2. The specimen was of uniform material, and fine and dense in particle composition. The diameter of the specimen was 50 mm, and the length was divided into three types. A specimen with a length of 100 mm was used for uniaxial compression and triaxial compression experiments, a specimen with a length of 50 mm was used for SHPB (split Hopkinson pressure bar) dynamic impact tests, and a specimen with a length of 25 mm was used for Split tensile tests. The specimens were finely ground at both ends of the test, and the non-parallelism was within 0.02 mm.

3.1. Determination of Basic Physical and Mechanical Parameters

The basic physical and mechanical parameters in the HJC model include density ρ, uniaxial compressive strength fc, elastic modulus E, Poisson's ratio ν, shear modulus G, and bulk modulus K. Among these parameters, the density is determined using the wax seal method. Uniaxial static compressive strength, maximum tensile hydrostatic pressure and corresponding strain were determined by uniaxial compression experiments, and other basic mechanical parameters were obtained using Formulas (10)–(14). The basic physical and mechanical parameters of diorite in the Jinan region are shown in Table 1.

$$E = \frac{\sigma_{\mathrm{E}}}{\varepsilon_{\mathrm{E1}}} \tag{10}$$

$$v = \frac{\varepsilon_{E2}}{\varepsilon_{E1}} \tag{11}$$

$$G = \frac{E}{2(1+v)} \tag{12}$$

$$K = \frac{E}{3(1-2v)} \tag{13}$$

$$T^* = \frac{T}{f_c} \tag{14}$$

Table 1. The basic physical and mechanical parameters of diorite.

ρ/ (kg·m^{-3})	f_c/ MPa	E/ GPa	ν	G/ GPa	K/ GPa	T/ MPa
3013	195.5	109.7	0.267	43.3	78.5	12.26

3.2. Determination of Strain Rate Constant

The strain rate constant C was determined using the SHPB test. To obtain the strain rate effect alone, the pressure effect must be removed. Figure 1 presents the technique used to remove the pressure effect and obtain the strain rate constant. Firstly, starting from the maximum hydrostatic pressure T^*($T^* = T/f_c = 0.063$), a straight line was drawn through each test date. Moreover, the slope of the straight line represented the strain A measure of the rate effect. Secondly, by making a straight line parallel to the vertical axis corresponding to the constant normalized pressure, $p^* = 1/3$, and intersecting the straight lines with different slopes. The characteristic strength under the same constant normalized pressure with different strain rates can be obtained, and the pressure effect was removed. The strain rate constant C is obtained by fitting the data points from the characterized stress at different strain rates, $C = 0.00103$, as shown in Figure 2.

3.3. Determination of Limit Surface Parameters

(1) Determination of strength constant A

If the effects of damage and strain rate are not considered, the limit surface equation of HJC model can be expressed as follows:

$$\sigma^* = A + BP^{*N} \tag{15}$$

Since Equation (15) does not consider the influence of the Rohde angle, the projection of the limit surface on the partial plane is the Mises circle. According to the plastic theory, when the Rhodes angle is 60°, the compression meridian of the Mises criterion on the deviated plane is connected to the compression meridian of the M-C criterion. The expression of the M-C criterion is expressed as shown in Formula (16).

$$\sigma = c + P\tan\varphi \tag{16}$$

In this equation, c and φ are cohesive strength and internal friction angle, respectively. According to the data of triaxial experimental under different confining pressures, an envelope of this group of Mohr circles was obtained, and the cohesive strength c is 49.12 MPa.

It can be seen from the above analysis that if the Mohr–Coulomb criterion satisfies the linear relationship, the strength constant A is equal to c/f_c, and the quasi-static cohesive strength (when $\dot{\varepsilon} = 10^{-4}/\mathrm{s}$) can be obtained at the same time, $A = 0.251$. When normalized strain rates $\dot{\varepsilon}^* = 1.0$, $A = 0.251/(1 + C\ln 10^{-4}) = 0.254$ were obtained.

(2) Determination of strength constants B and N

Triaxial compression tests were performed using a triaxial compression apparatus. Under different confining pressure conditions, according to Formulas (17) and (18), the different hydrostatic pressures p and the corresponding maximum differential pressure $\Delta\sigma$ are measured. Normalizing maximum differential pressure $\Delta\sigma$ as shown in Formula (19), a series of points (P^*,σ^*) was obtained. Then, to obtain the values of the strength constants B and N, the data points were fitted as shown in Formula (20).

$$P = \frac{\sigma_1 + 2\sigma_3}{3} \tag{17}$$

$$\Delta\sigma = \sigma_1 - \sigma_3 \tag{18}$$

$$\sigma^* = \frac{\Delta\sigma}{f_c} \tag{19}$$

$$\sigma^* = 0.254 + BP^{*N} \tag{20}$$

Figure 3 shows the test data and fitting results. The strength constants B and N are 1.695 and 0.742, respectively.

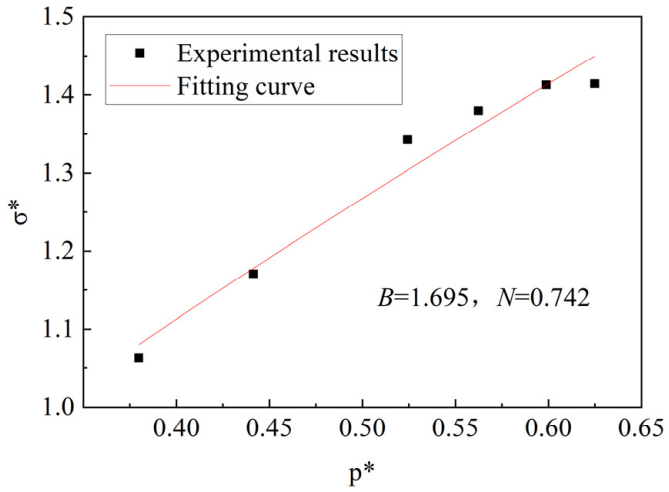


Figure 3. Technique for determining strength constants B and N.

3.4. Determination of State Equation Parameters

The pressure constants of diorite are as follows:

$$P_{crush} = f_c/3 = 65.169 \text{ MPa} \tag{21}$$

$$\mu_{crush} = P_{crush}/K = 0.000831 \tag{22}$$

$$\mu_{lock} = \frac{\rho_g}{\rho_0} - 1 = 0.00204 \tag{23}$$

where ρ_g and ρ_0 are grain density and real density respectively.

The values of $K1$, $K2$, and $K3$ can be obtained from the Hugoniot test for diorite. The parameters are derived from the existing research results and obtained by fitting, as shown in Figure 4. Based on the fitting results, $K1$ = 94.7 GPa, $K2$ = 632.4 GPa, $K3$ = 938.1 GPa. p_{lock} = 2.2 GPa is the pressure at which all the air voids are removed from the rock. p_{lock} is determined by providing the best fit to the data.

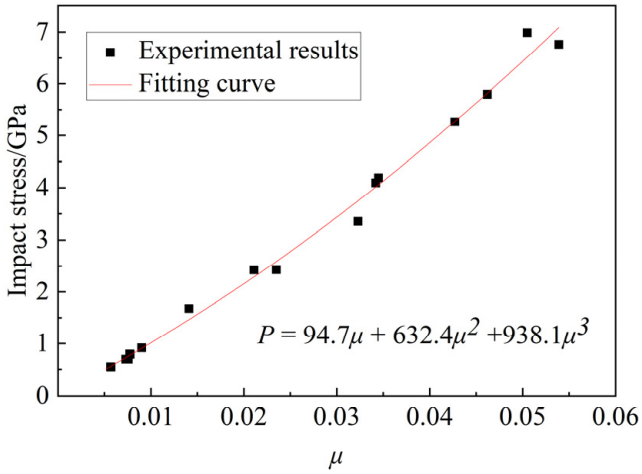


Figure 4. Description of data processing method for the values of *K*1, *K*2, *K*3.

3.5. Determination of Damage Model Constants

Figure 5 shows the stress–strain results for a cylinder subjected to SHPB cyclic compression loading test. An assumed failure surface is defined on the basis of the test results. The tangent line from the failure surface intersects with the x-axis, and the intersection point is EF_{min}. The value of EF_{min} is 0.00977, as shown in Figure 5.

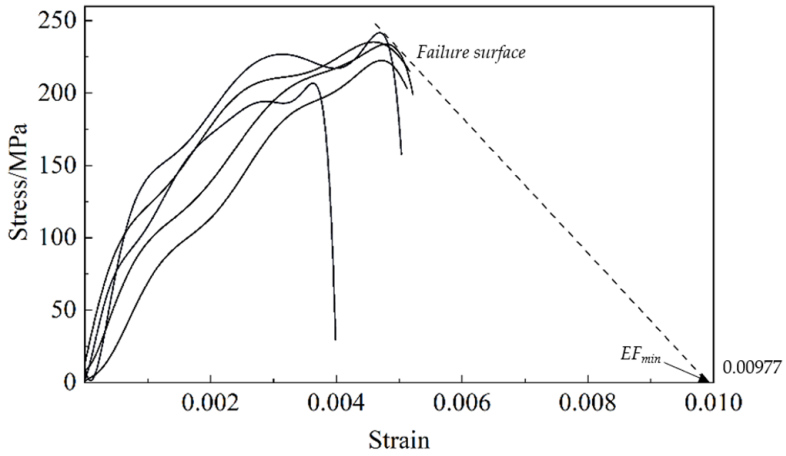


Figure 5. Technique for obtaining the value of EF_{min}.

Previous studies have shown that D_2 has little effect on the results. Therefore, following the previous calculation method, first assume that $D_2 = 1.0$, then determine the value of D_1 according to Formula (3), $D_1 = 0.0312$.

4. Numerical Simulation Results and Discussion

4.1. Design of Numerical Model

The numerical simulation model of rock breaking using a disc cutter performed in this study was established using the LS-DYNA module in ANSYS. Figure 6 shows the model of rock breaking using a disc cutter. The simulation uses a disc cutter with a diameter of 457.2 mm (18 inches). To be closer to the actual rock-breaking behaviour of the disc cutter, the cutter model is divided into two parts, one is the cutter ring, and the other is the cutter body. In this study, the cutter ring is an elastic body, and the cutter body is a rigid body. The two are in contact with each other, but not fixed to ensure that the outer cutter ring can be rotated during the rock-breaking process, as shown in Figure 7. The rotation depends on the friction between the disc cutter and the rock, which is more in line with the actual behaviour of the disc cutter. The disc cutter model parameters are shown in Table 2.

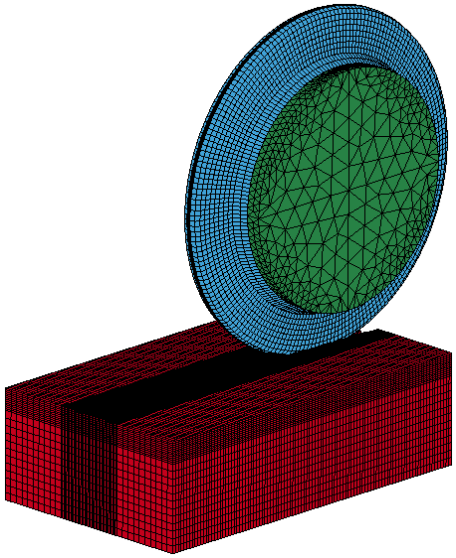


Figure 6. Model of rock breaking by disc cutter.

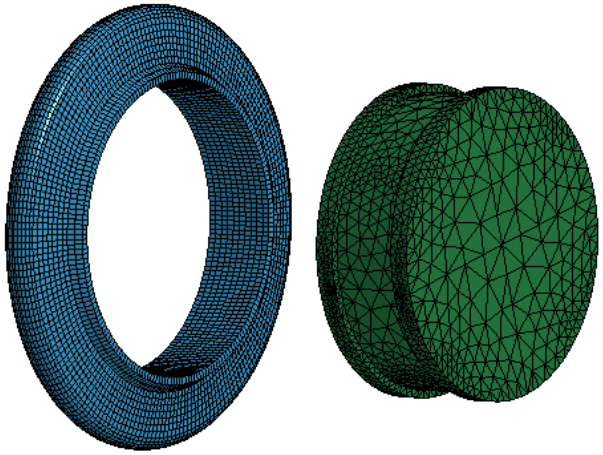


Figure 7. Cutter ring and cutter body.

Table 2. Disc cutter material characteristic parameters.

Category	Density (kg/m^3)	Young's Modulus (GPa)	Poisson's Ratio
Cutter ring	7850	209	0.3
Cutter body	7830	207	0.3

In this study, the rock mass is designed as a rectangle with length, width and height of 500 mm, 300 mm and 150 mm, respectively, as shown in Figure 8. The constitutive relation selected for the rock in the numerical simulation of rock breaking using a disc cutter is the HJC model of the diorite of the Jinan region, and the characteristic parameters of the HJC model are shown in Table 3. The contact between the cutter ring and the rock mass corresponds to eroding contact.

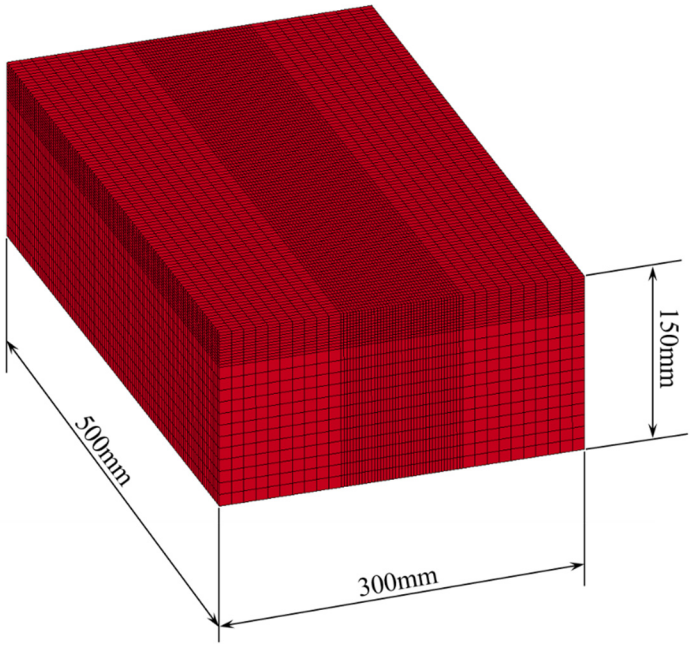


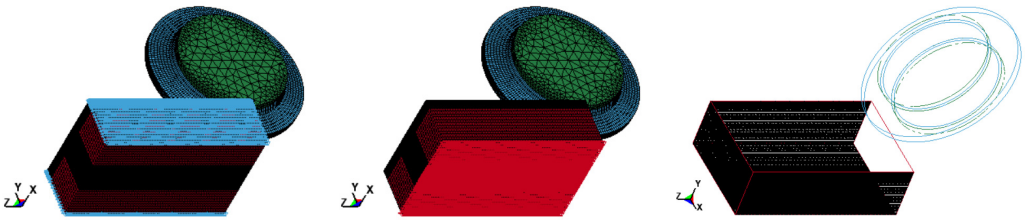
Figure 8. Schematic diagram of rock materials.

Table 3. Diorite's HJC model characteristic parameters.

Parameters Type	Symbol	Value	Unit
Basic parameters	ρ	3013	kg/m^3
	G	43.3	GPa
	T	12.26	MPa
	f_c	195.5	MPa
Strain rate constants	C	0.00103	
	$ESPO$	1.0	
Limit surface parameters	A	0.254	
	B	1.695	
	N	0.742	
	S_{FMAX}	1.42	
State equation parameters	P_{crush}	65.169	MPa
	P_{lock}	2.2	GPa
	μ_{crush}	0.000831	
	μ_{lock}	0.00204	
	$K1$	94.7	GPa
	$K2$	632.4	GPa
	$K3$	938.1	GPa
Damage model constant	$D1$	0.0312	
	$D2$	1	
	EF_{min}	0.00977	

In terms of boundary conditions, the displacement in the x direction of the two sides of the rock is limited, and the bottom surface restricts the displacement and rotation in all directions, as shown in Figure 9a,b. Non-reflective boundaries are set on two sides, the bottom face and the face in front of the disc cutter forward direction, as shown in Figure 9c. For the disc cutter, translational and rotational constraints in two directions (x, y) other than the forward direction are set, so that the disc cutter can maintain its penetration and avoid deviating from the predetermined trajectory. In terms of rock breaking, an additional keyword (MAT_ADD_EROSION) is set for the HJC model, which allows each unit of the rock to be deleted after its maximum principal strain reaches a predetermined value. The

parameter settings are shown in Figure 10. In addition, the standard crack initiation and crack growth model are not considered in the present work, and will be discussed in depth in follow-up studies. The contact properties between the cutter and the rock correspond to eroding contact (surface to surface); the static coefficient of friction between the two is 0.35, and the dynamic coefficient of friction is 0.18, as shown in Figure 11.



(**a**) (**b**) (**c**)

Figure 9. Boundary conditions of the rock mass. (**a**) Constraints in the two side; (**b**) Constraints in the bottom; (**c**) Non-reflective boundaries.

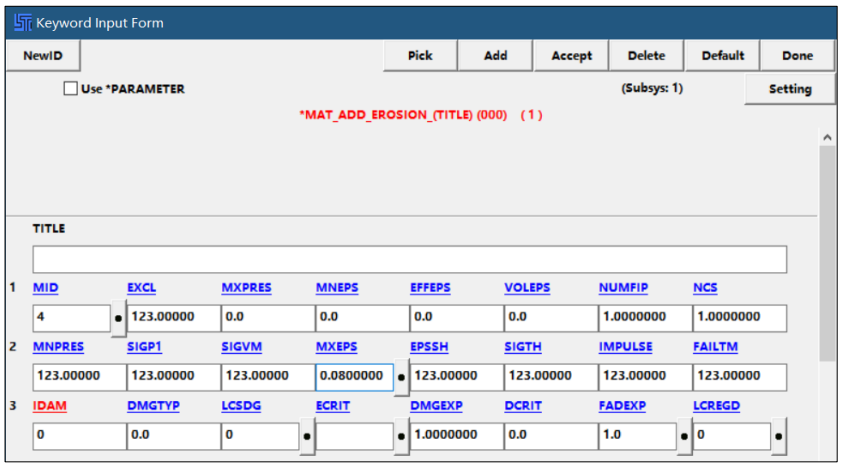


Figure 10. Keyword-MAT_ADD_EROSION.

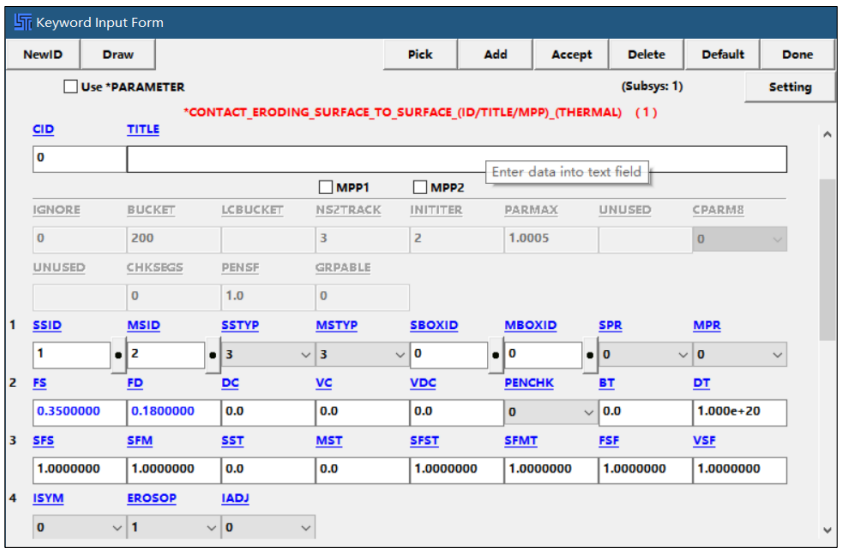


Figure 11. Contact properties between cutter and rock.

4.2. Numerical Simulation Results and Discussion

To figure out the influence of blade width (BW) and blade fillet (BF) on the disc cutter when breaking rock, 14 different blade types of disc cutters with combinations of four different blade widths (19 mm, 22 mm, 25 mm, and 28 mm) and six different blade fillets (0 mm, 5 mm, 9 mm, 10 mm, 13 mm, and 15 mm) were established. In addition, the force of these 14 types of disc cutter were discussed under different penetration and speed conditions. These 14 kinds of disc cutter are shown in Figure 12.

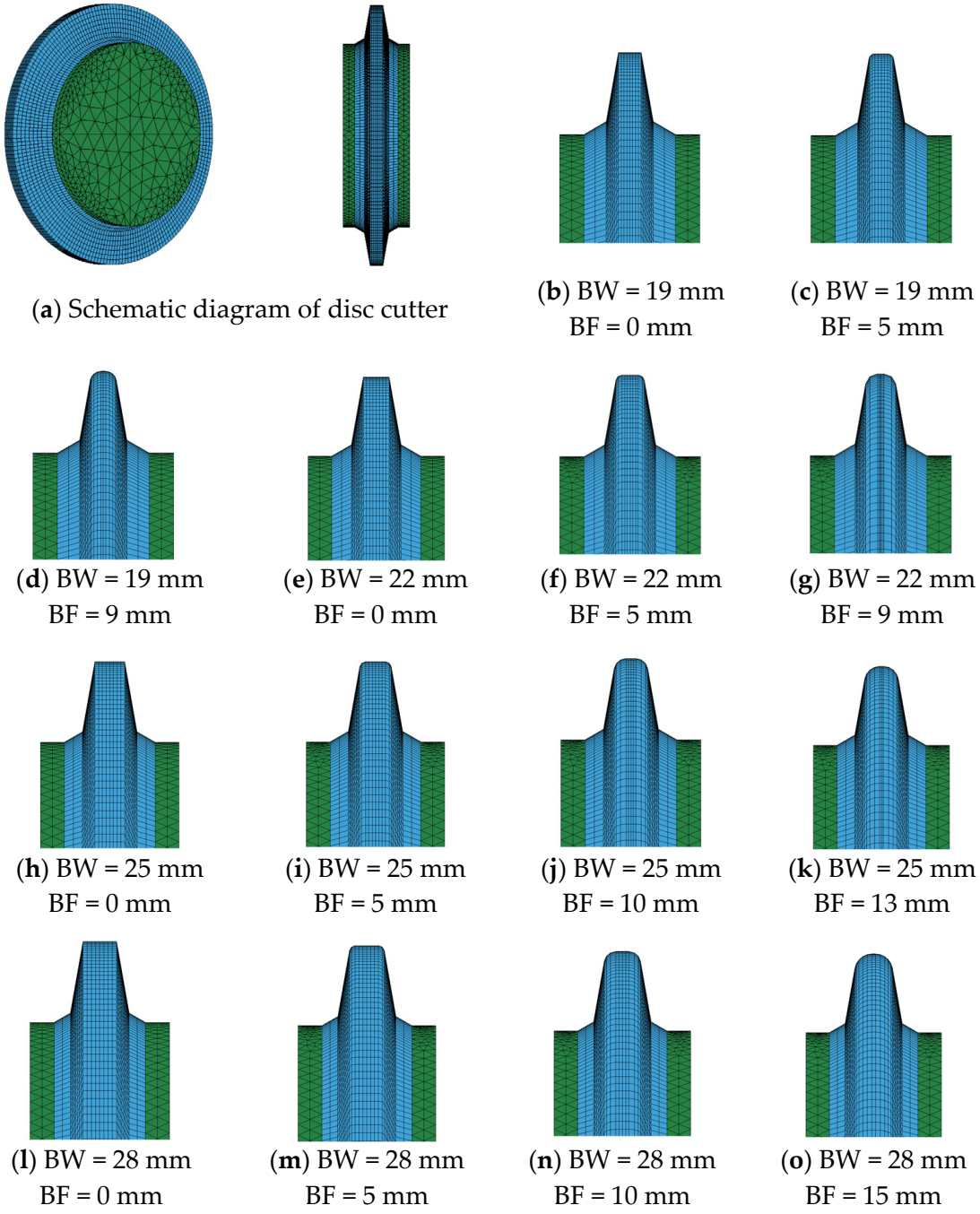


Figure 12. Fourteen different blade types of disc cutters.

From LS-DYNA, the contact force between the disc cutter and the rock at each moment can be extracted, and the range and standard deviation can be calculated on the basis of the extracted contact force. The steps to extract contact force are shown in Figures 13–15.

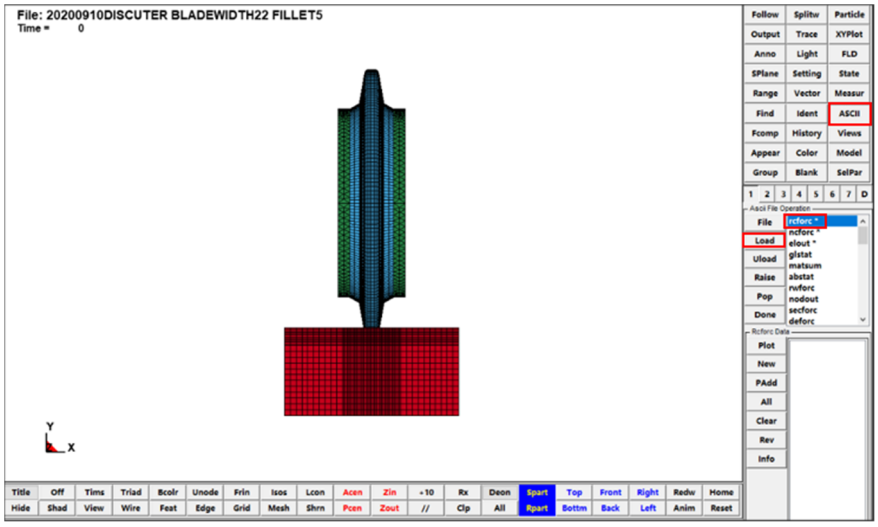


Figure 13. Load RCFORCE into the model.

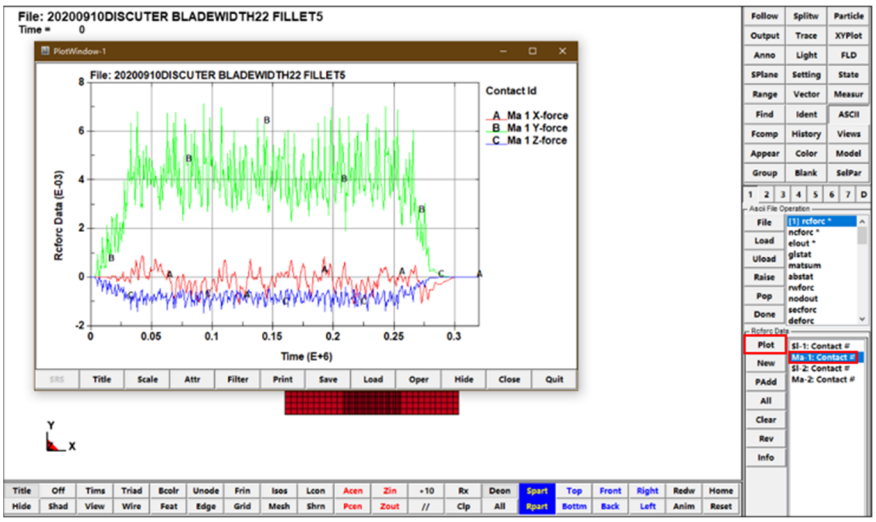


Figure 14. Plot the contact force.

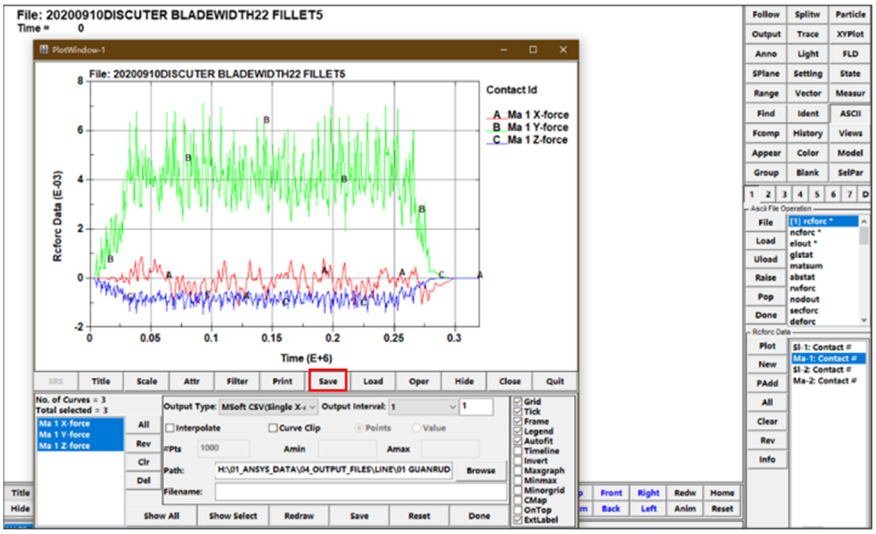


Figure 15. Save contact force data in EXCEL format.

4.2.1. Comparison of Blade Fillet

Figure 16 shows the contact force, contact force range and standard deviation of three kinds of disc cutter with the same blade width (22 mm) and different blade fillets (0, 5 and 9 mm) at different penetration depths (5, 10, 15, 20 and 25 mm). From Figure 16a,b, it can be seen that with increasing penetration, the contact force of the three kinds of disc cutter gradually increase. It is also obvious that, with the same penetration depth, the larger the blade fillet, the smaller the contact force. As can be seen from Figure 16c,d, with increasing penetration, the standard deviation of the contact force changes little and is relatively stable, but the range of contact force fluctuates slightly and increases. We can see that with increasing blade fillet, the range and standard deviation of the contact force both decrease. It can be seen that the disc cutter with a 22 mm blade width and a 9 mm blade fillet performs better in various indicators.

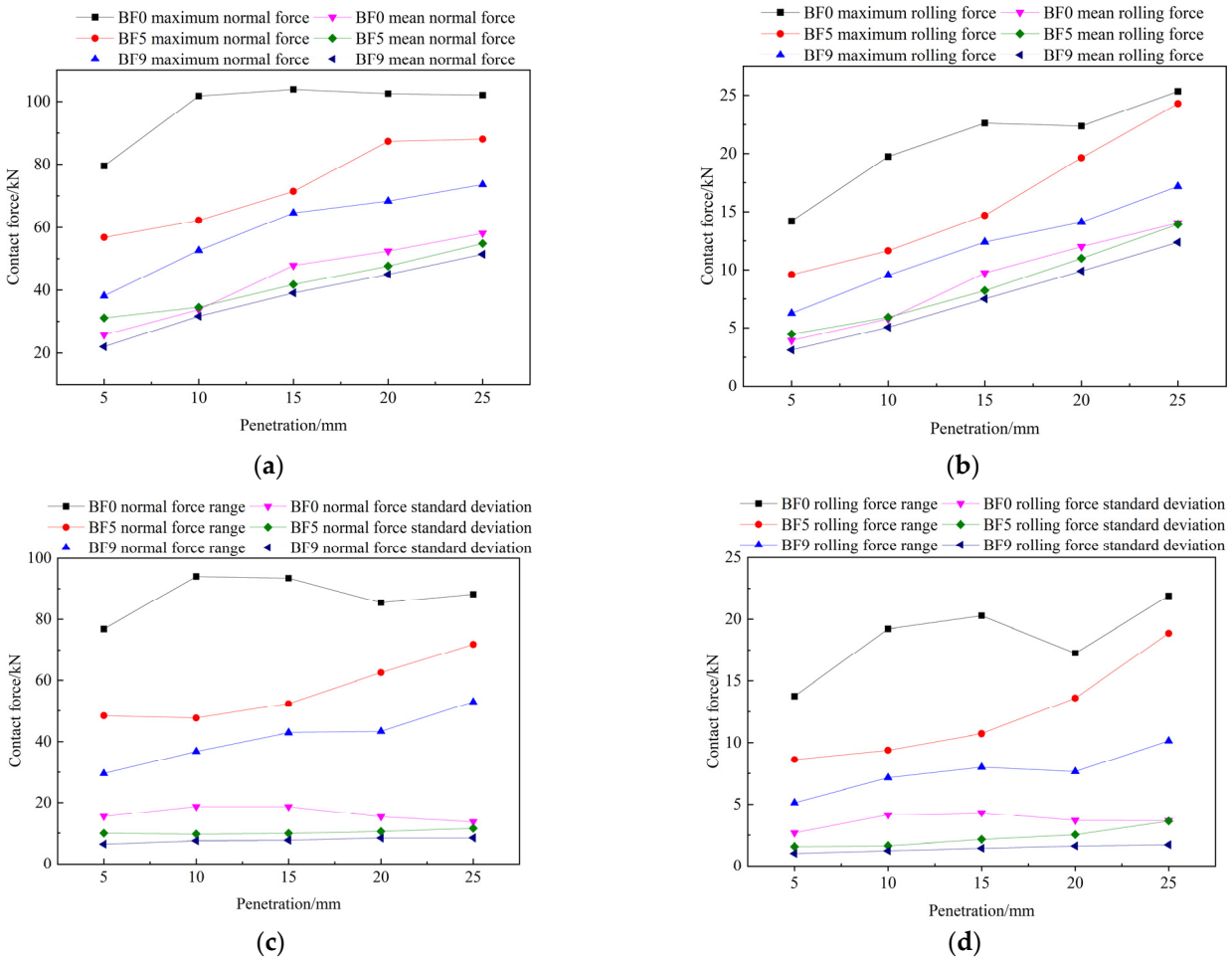


Figure 16. The contact force of BW 22mm disc cutter with different blade fillets. (**a**) Normal force; (**b**) Rolling force; (**c**) Range and STD of normal force; (**d**) Range and STD of rolling force.

Figures 17 and 18 show the equivalent stress and stress contour of rock breaking using three kinds of disc cutter with different blade fillets and a 22 mm blade width. It can be seen that the influence range of the disc cutter during rock breaking decreases with increasing blade fillet. In addition, the shape of the influence range gradually transitions from an approximate circle to a trapezoid and finally a triangle.

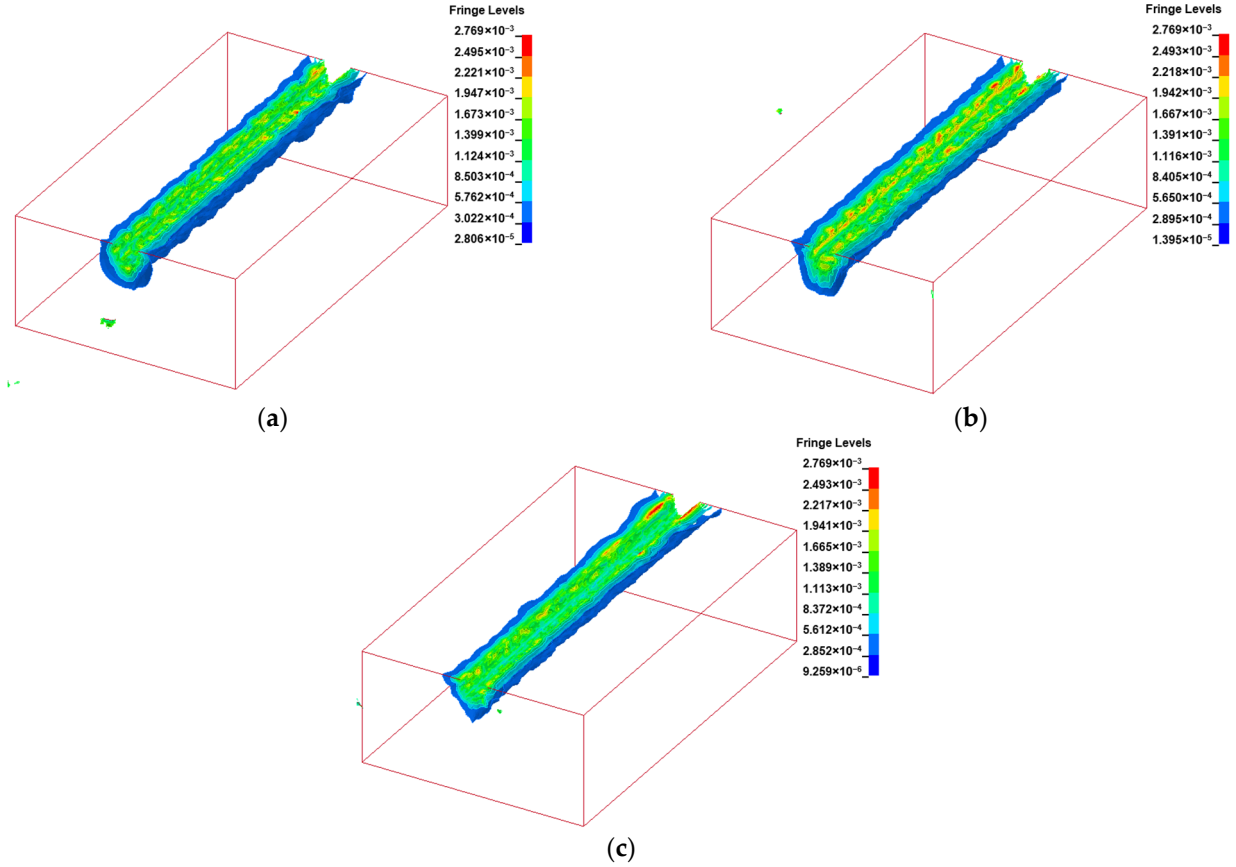


Figure 17. Equivalent stress isosurface of rock breaking using disc cutter with 22 mm blade width. (**a**) Isosurface of equivalent stress (Blade fillet 0 mm); (**b**) Isosurface of equivalent stress (Blade fillet 5 mm); (**c**) Isosurface of equivalent stress (Blade fillet 9 mm).

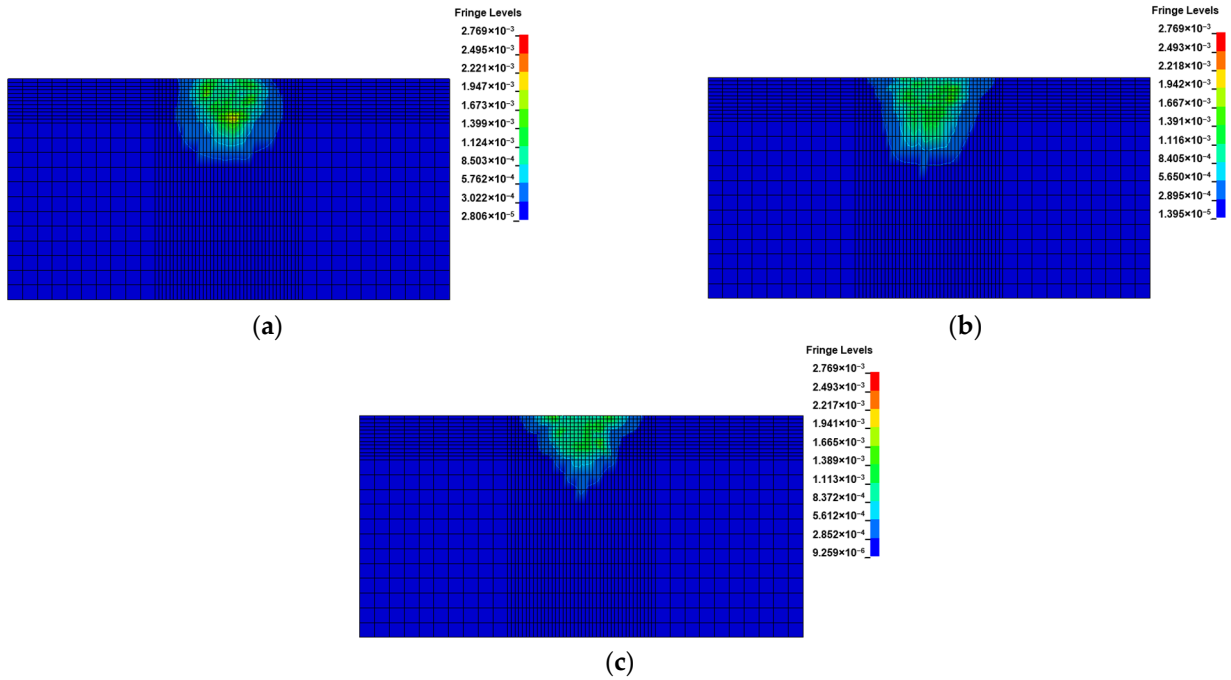


Figure 18. Stress contour of rock breaking by disc cutter with 22 mm blade width. (**a**) Stress contour of rock breaking (Blade fillet 0 mm); (**b**) Stress contour of rock breaking (Blade fillet 5 mm); (**c**) Stress contour of rock breaking (Blade fillet 9 mm).

4.2.2. Comparison of Blade Width

Figure 19 shows the contact force, contact force range and standard deviation of four kinds of disc cutter with the same blade fillet (5 mm) and different blade widths (19, 22, 25 and 28 mm) at different penetration depths (5, 10, 15, 20 and 25 mm). It can be seen from Figure 19a,b that with the same blade fillet, the wider the blade width, the greater the contact force. As can be seen from Figure 19c,d, with the same penetration, the range and standard deviation of contact force both increase with increasing blade width.

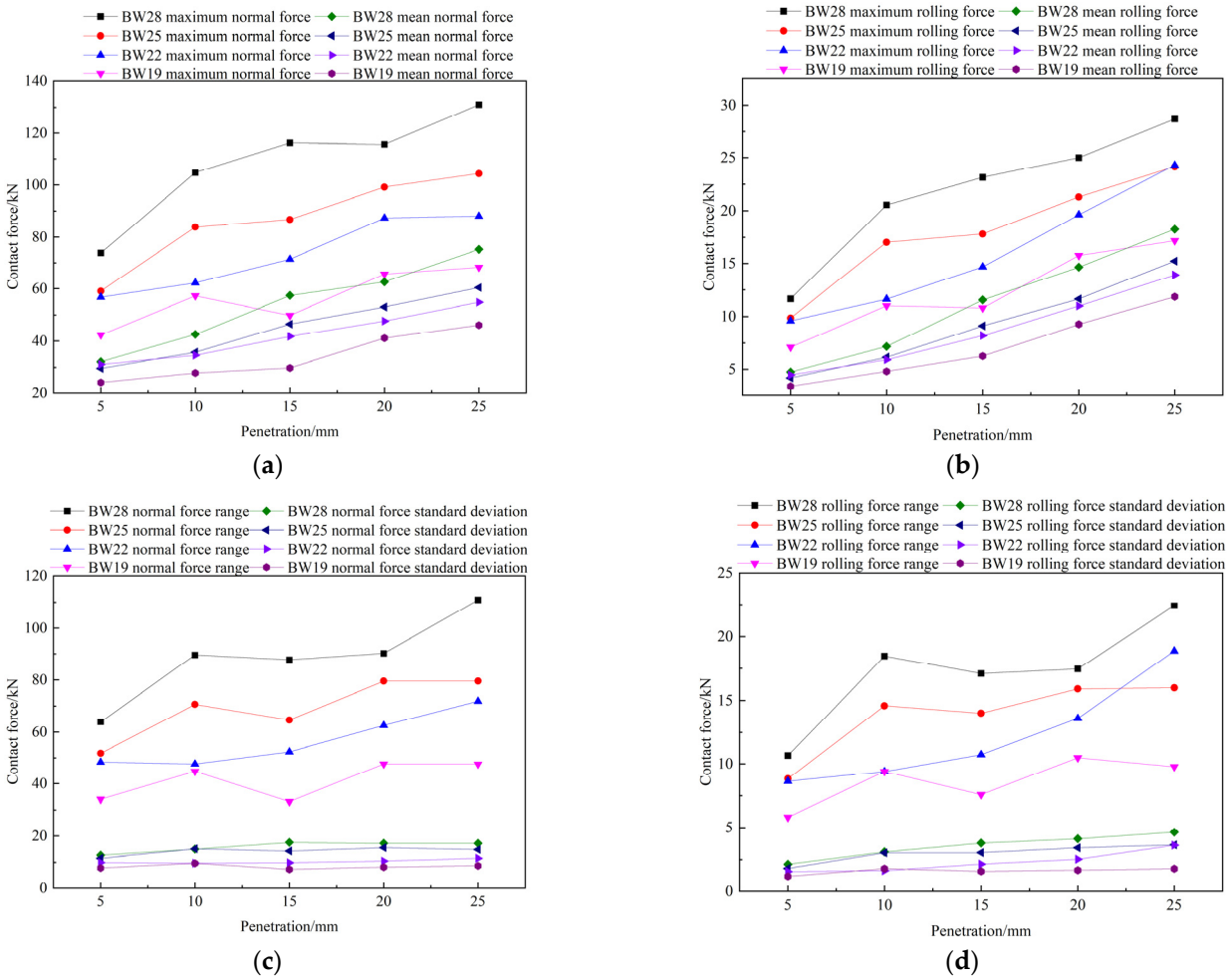


Figure 19. The contact force of BF 5mm disc cutter with different blade widths. (**a**) Normal force; (**b**) Rolling force; (**c**) Range and STD of normal force; (**d**) Range and STD of rolling force.

Figures 20 and 21 show the equivalent stress and stress contour of rock breaking using four kinds of disc cutter with different blade widths and a 5 mm blade fillet. It can be seen that the influence range of the disc cutter during rock breaking increases with increasing blade width. At the same time, the shapes of the rock-breaking influence range with the disc cutter under the four different blade widths are all trapezoid.

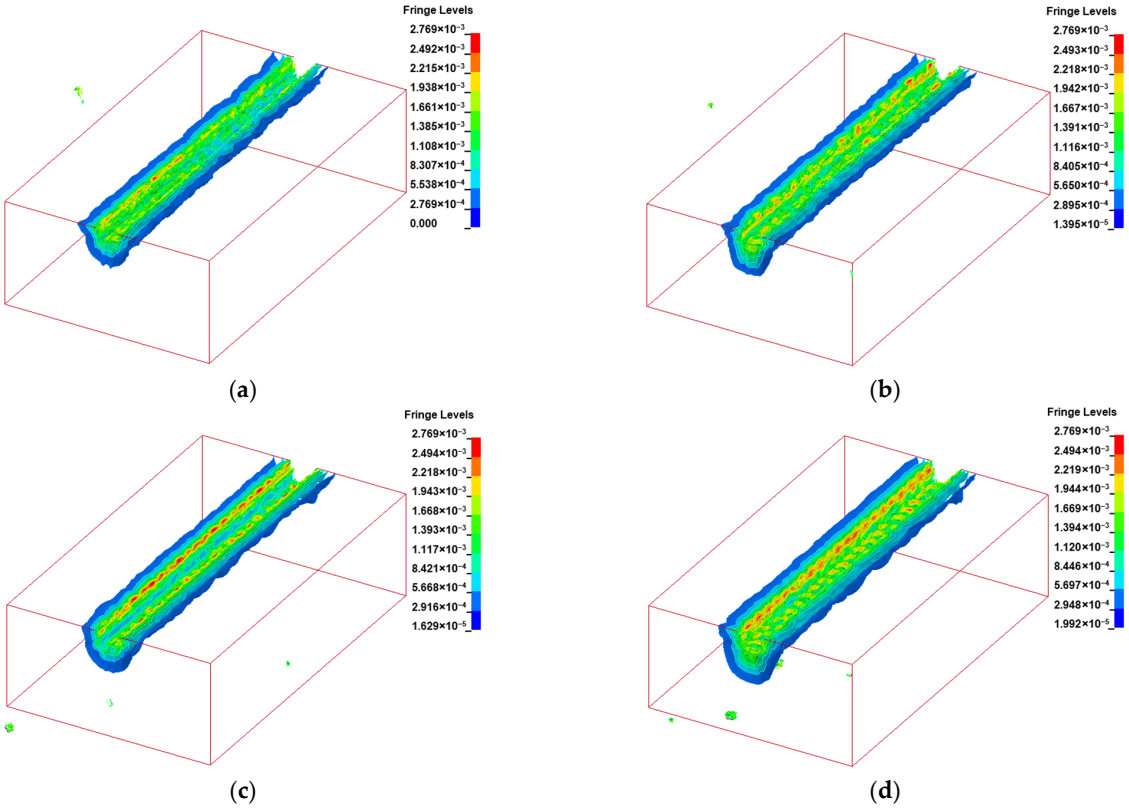


Figure 20. Equivalent stress isosurface of rock breaking using disc cutter with 5 mm blade fillet. (**a**) Isosurface of equivalent stress (Blade width 19 mm); (**b**) Isosurface of equivalent stress (Blade width 22 mm); (**c**) Isosurface of equivalent stress (Blade width 25 mm); (**d**) Isosurface of equivalent stress (Blade width 28 mm).

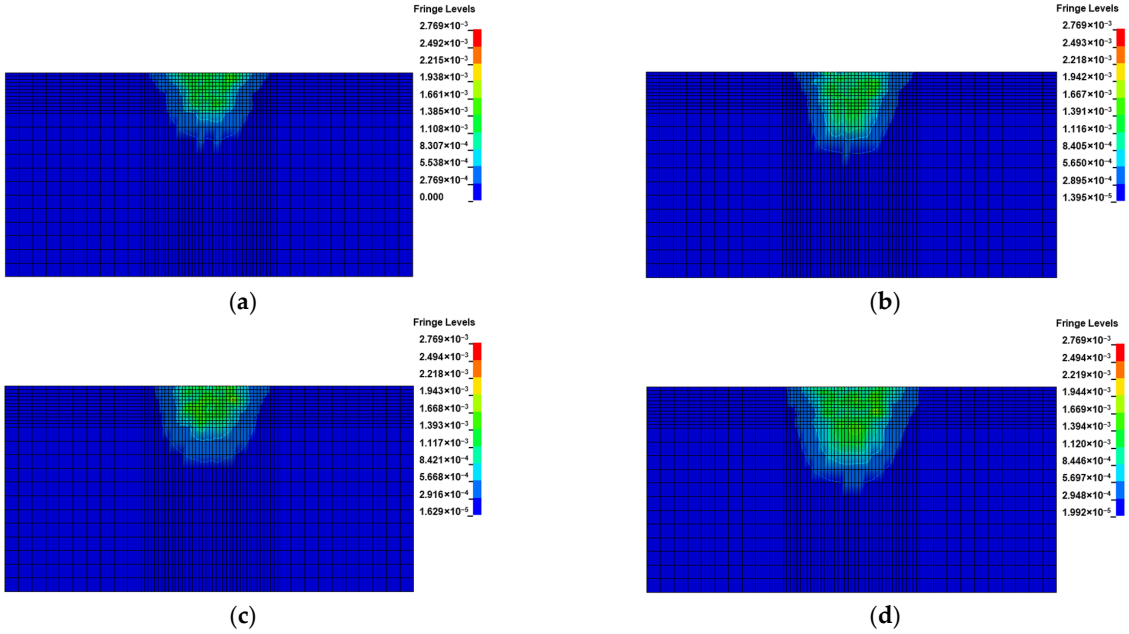


Figure 21. Stress contour of rock breaking using disc cutter with 5 mm blade fillet. (**a**) Stress contour of rock breaking (Blade width 19 mm); (**b**) Stress contour of rock breaking (Blade width 22 mm); (**c**) Stress contour of rock breaking (Blade width 25 mm); (**d**) Stress contour of rock breaking (Blade width 28 mm).

5. Discussion

It can be seen in Figure 16a,b that, among the three types of disc cutter with different blade fillets and a blade width of 22 mm, the contact force of the disc cutter with a blade fillet of 0 mm was smaller than that of the disc cutter with a blade fillet of 5 mm and larger than that of the disc cutter with a blade fillet of 9 mm when the penetration was 5 mm. Its growth rate was faster, and its contact force was obviously greater than that of the other two kinds of disc cutter when the penetration exceeded 10 mm. When the penetration was 5 mm, the contact force of the disc cutter with a blade fillet of 5 mm was greater than that of the others, but with increasing penetration, the increment in the contact force was smaller, and the growth rate was relatively stable. The contact force of the disc cutter with a blade fillet of 9 mm was smaller than that of the others under all penetration conditions, and with increasing penetration, its increment was relatively stable and approximately linear.

It can be seen in Figure 16c,d that the range and standard deviation of the contact force of the disc cutter with a blade fillet of 0 mm was significantly greater than that of the other two kinds of disc cutter with different blade fillets. The range of the contact force of the disc cutter with a blade fillet of 5 mm increased slightly when the penetration was increased from 5 mm to 15 mm, and then increased rapidly. In addition, its standard deviation changed slightly with increasing penetration. The growth trend of the range and standard deviation of the contact force of the disc cutter with a blade fillet of 9 mm were similar to those of the disc cutter with a blade fillet of 5 mm, but the values were lower.

According to the analysis of the contact force of the three kinds of disc cutter with different blade fillets and a blade width of 22 mm under different penetration depths, it can be seen that the contact force of the disc cutter with a blade fillet of 0 mm was relatively large during the rock breaking process. Moreover, the contact force fluctuated more violently than in the other cases. Although the influence range of the disc cutter during rock breaking was larger than that of the other two types of disc cutter, it was easy for damage to be caused to the cutter due to the more violent cyclic loading in the actual use process. The contact force of the disc cutter with a blade fillet of 5 mm was greater than that of the disc cutter with a blade fillet of 9 mm at all penetration depths, and their growth trends were similar. The range of contact force and standard deviation both increased with increasing penetration, and were both larger than those of the disc cutter with a blade fillet of 9 mm. However, the increment in standard deviation was relatively small, and the growth rate was relatively stable. The contact force, range and standard deviation of the disc cutter with a blade fillet of 9 mm were smaller than those of the other two kinds of disc cutter under different penetration depths. The contact force range increased with increasing penetration. In addition, the standard deviation of contact force remained basically unchanged with increasing penetration, so the fluctuation in the contact force of this kind of disc cutter was the smallest among these disc cutters under different penetration depths, but the influence range of the disc cutter during rock breaking was also relatively small.

It can be seen from Figure 19 that, among the four types of disc cutters with 5 mm blade fillets and different blade widths, the disc with a blade width of 19 mm showed a small increase in contact force with penetration within the range of 5–15 mm. The increase in the contact force of the three other kinds of disc cutter was relatively consistent, but it can be clearly seen that the contact force increases with increasing blade width. In addition, the range and standard deviation of the contact force of the disc with a blade width of 19 mm were smaller than those of the other three kinds of disc cutter. Although the range of the contact force increased in a fluctuating manner with increasing penetration depth, the overall growth rate was low. The contact force range of the disc cutter with a blade width of 22 mm increased approximately linearly with increasing penetration, with a relatively stable growth trend, and the standard deviation of the contact force was closer to that of the disc cutter with a blade width of 19 mm. The contact force range of the disc cutters with blade widths of 25 mm and 28 mm generally showed a near-linear growth trend, and the standard deviation of their growth trend was relatively stable. However, the overall values of range and standard deviation were obviously greater than those of the disc cutters with

blade widths of 19 mm and 22 mm. In terms of the influence range of the disc cutter during rock breaking, it can be clearly seen that the influence range increased with increasing blade width, but the shape remained basically unchanged.

At present, most of the research on shield disc cutters is focused on the influence of the shield tunnelling parameters on the rock-breaking behaviour of the disc cutter. In this paper, the influence of the geometric configuration of a single disc cutter on rock-breaking behaviour was analysed in detail, in order to be able to provide certain guidelines for the selection of disc cutters during shield tunnel construction. Although founded on a study of a single disc cutter, this is only a small part of the total rock-breaking behaviour of the shield machine, and therefore the rock-breaking behaviour of the group of disc cutters present in the cutter-head should be further explored. In follow-up research, in order to validate the rock-breaking behaviour of a single disc cutter, a more detailed and systematic study of the rock-breaking behaviour of groups of disc cutters will be carried out.

In the current rock-breaking simulation of a shield disc cutter, the HJC model was used as the constitutive model for the rock. However, previous studies have seldom determined the parameters of the HJC model of the targeted rock, rather mainly opting to use existing HJC models. In addition, most of the parameters are taken from the concrete HJC model. In this paper, the parameters of the HJC constitutive model were determined for the diorite in the Jinan area, so the simulation results are more accurate and closer to the actual situation in engineering practice.

The HJC model is used for the simulation of rock and concrete under large deformation and high strain rates. In the early stage, it was mainly used in high-speed interactions such as bullet–concrete penetration. For the rock-breaking behaviour of the disc cutter, the speed of the disc cutter is relatively slow (the running speed of the disc cutter is generally ≤ 2 m/s), so the HJC model has certain limitations when simulating rock-breaking behaviour in the cutter–rock interaction, and is different from the actual situation. Therefore, in follow-up research, a new constitutive model should be developed according to the characteristics of the rock-breaking behaviour of the disc cutter to ensure a better match between the simulation and the actual construction.

In the actual shield construction, the disc cutter can easily maintain a penetration of about 10 mm in soft and medium-hardness rock formations (strength less than 30 MPa). In hard rock formations (strength greater than 50–100 MPa), penetration is generally 5–10 mm. However, it is difficult for the disc cutter to penetrate the rock, and the penetration is difficult to maintain. In extremely hard rock formations (strength greater than 120 MPa) and soft–hard mixed formations, it is difficult to penetrate the rock and the damage to the disc cutter will be more serious. At the same time, in order to reduce the amount of cutter damage, the penetration degree is generally maintained below 5 mm, and in most cases even less than 3 mm. Combined with the actual construction situation and the relevant research content in this paper, we give several basic suggestions for the configuration of disc cutters in different strata:

- In soft and medium-hardness rock formations, the cutter penetrates easily, so the rock-breaking efficiency of the disc cutter should be improved as much as possible. This means that the rock-breaking influence range of the disc cutter should be increased. Therefore, it is recommended to use a disc cutter with a large blade width (25–28 mm) and a small blade fillet (0–5 mm);
- In hard rock formations, it is difficult for the disc cutter to penetrate, so the ability of the disc cutter to penetrate the rock should be ensured. This will result in a reduction in the penetration force. Therefore, a disc cutter with a medium or small blade width (19–22 mm) and a medium blade fillet (9–10 mm) should be selected;
- In extremely hard rock formations and soft–hard mixed formations, it is hard to penetrate the rock and the damage to the cutter is serious, so a balance between the life of the disc cutter and penetration ability should be found. Therefore, it is appropriate to use a disc cutter with a large blade width (28 mm) and a large blade fillet (15 mm).

6. Conclusions

This study mainly focuses on two aspects. First, to ensure the accuracy and validity of the numerical simulation, the parameters of the diorite HJC model in the Jinan area were determined. Secondly, the numerical simulation of a disc cutter with different blade widths and blade fillets was carried out using the parameters of the diorite HJC model in the Jinan area. The main conclusions of this study are enumerated below.

(1) The basic physical and mechanical parameters, the strain rate constant, the limit surface parameters, state equation parameters and damage model constants of diorite in the Jinan region were obtained by means of a series of experiments. Compared with previous numerical simulation studies on rock-breaking using disc cutters, this study obtained simulation results closer to the actual situation by measuring the rock parameters encountered in the actual project.

(2) The influence of the penetration degree on the contact force of the disc cutter and its range and standard deviation were investigated. With increasing penetration, the contact force of the disc cutter gradually increases, and the range of contact force fluctuates slightly and increases, but the standard deviation of the contact force remains stable.

(3) The influence of blade fillet and blade width on the rock-breaking behaviour of the disc cutter was analysed. When the penetration was the same, the larger the blade fillet, the smaller the contact force, as well as the range and the standard deviation of contact force. The influence range of the disc cutter during rock breaking decreases with increasing blade fillet. At the same penetration depth, the wider the blade width, the greater the contact force, range of contact force and standard deviation of contact force. Moreover, the influence range of the disc cutter during rock breaking increases with increasing blade width.

(4) The influence law of each factor described in this paper on the rock-breaking behaviour of the disc cutter provides a certain reference for the selection of disc cutters in future shield projects.

It is hoped that the research on the influencing factors of rock-breaking by disc cutters in this paper will be able to provide a certain reference for engineering in the construction of shield tunnels. The current research is mainly limited to the rock-breaking simulation of a single disc cutter, with the simulated cutter being an 18-inch disc cutter, and the research results were not further verified by laboratory experiments. In future research, the rock-breaking behaviour of 17–20 inch disc cutters should be explored extensively and in detail, in order to provide more effective and specific guidance for practical engineering. At the same time, research on the rock-breaking behaviour of groups of disc cutters should be carried out, and the overall rock-breaking ability and rock-breaking effect of the shield should be further discussed in a more macro and specific manner.

Author Contributions: Methodology, Y.D.; Software, J.W.; Investigation, X.D.; Resources, B.W. and Z.S.; Funding acquisition, D.Y. All authors have read and agreed to the published version of the manuscript.

Funding: This work was supported by Shandong Provincial Key Research and Development Program [grant numbers No. 2021CXGC010209]; the National Natural Science Foundation of China [grant numbers No. 52278389]; and the Ministry of Housing and Urban-Rural Development [grant numbers No. 2020-K-142].

Institutional Review Board Statement: Not applicable.

Informed Consent Statement: Not applicable.

Data Availability Statement: The data presented in this study are available from the corresponding author upon request.

Conflicts of Interest: The authors declare that they have no conflict of interest to report regarding the present study.

References

1. Fang, Q.; Liu, X.; Zeng, K.; Zhang, X.; Zhou, M.; Du, J. Centrifuge modelling of tunnelling below existing twin tunnels with different types of support. *Undergr. Space* **2022**, *7*, 1125–1138. [CrossRef]
2. Zheng, H.; Li, P.; Ma, G.; Zhang, Q. Experimental investigation of mechanical characteristics for linings of twins tunnels with asymmetric cross-section. *Tunn. Undergr. Sp. Tech.* **2022**, *119*, 104209. [CrossRef]
3. Zhang, J.; Zhang, D.; Huang, H.; Phoon, K.K.; Tang, C.; Li, G. Hybrid machine learning model with random field and limited CPT data to quantify horizontal scale of fluctuation of soil spatial variability. *Acta Geotech.* **2022**, *17*, 1129–1145. [CrossRef]
4. Zhang, J.; Phoon, K.K.; Zhang, D.; Huang, H.; Tang, C. Novel approach to estimate vertical scale of fluctuation based on CPT data using convolutional neural networks. *Eng. Geol.* **2021**, *294*, 106342. [CrossRef]
5. Geng, Z.; Jin, D.; Yuan, D. Face stability analysis of cohesion-frictional soils considering the soil arch effect and the instability failure process. *Comput. Geotech.* **2023**, *153*, 105050. [CrossRef]
6. Yuan, D.; Jun, W.; Xiang, S.; Jin, D.; Li, X. Engineering Safety of Cross-River or Cross-sea Long-distance Large-diameter Shield Tunneling Under Superhigh Water Pressure. *China J. Highw. Transp.* **2020**, *33*, 26–45. (In Chinese)
7. Jin, D.; Yuan, D.; Li, X.; Su, W. Probabilistic analysis of the disc cutter failure during TBM tunneling in hard rock. *Tunn. Undergr. Sp. Tech.* **2021**, *109*, 103744. [CrossRef]
8. Wang, X.; Yuan, D.; Jin, D.; Jin, H.; Yang, Y.; Wu, J. Determination of thrusts for different cylinder groups during shield tunneling. *Tunn. Undergr. Sp. Tech.* **2022**, *127*, 104579. [CrossRef]
9. Acaroglu, O.; Ozdemir, L.; Asbury, B. A fuzzy logic model to predict specific energy requirement for TBM performance prediction. *Tunn. Undergr. Sp. Tech.* **2008**, *23*, 600–608. [CrossRef]
10. Wu, Q.X.; An, G.F.; Zhou, X.W.; Chen, L. Numerical Simulation of Rock Breaking by Disc Cutter of Tunnel Boring Machine. *Appl. Mech. Mater.* **2014**, *638–640*, 888–893. [CrossRef]
11. Li, H.; Du, E. Simulation of rock fragmentation induced by a tunnel boring machine disk cutter. *Adv. Mech. Eng.* **2016**, *8*, 756494043. [CrossRef]
12. Hu, X.; Jiang, H.; Du, C. Finite Element Method for Prediction of Rock Breaking Performance of the Tipped Hob With Different Tooth Profiles. *IEEE Access* **2020**, *8*, 50421–50430. [CrossRef]
13. Holmquist, T.J.; Johnson, G.R.; Cook, W.H. A computational constitutive model for concrete subjective to large strain, high strain rates, and high pressure. In Proceedings of the 14th International Symposium on Ballistic, Quebec City, QC, Canada, 26–29 September 1993.
14. Johnson, G.R.; Beisse, S.R.; Holmquist, T.J.; Frew, D.J. Computer radial stresses in a concrete target penetrated by a steel projectile. In *Proceedings of Structures under Shock and Impact V*; Aristotle University of Thessaloniki: Thessaloniki, Greece, 1998.
15. Zhang, F.; Li, E. A method to determine the parameters of the model for concrete impact and damage. *J. Ballist.* **2001**, *13*, 12–16. (In Chinese)
16. Polanco-Loria, M.; Hopperstad, O.S.; Berstad, T.; Børvik, T. *Ballistic Limit Assessments for Concrete Slabs Using the MHJC Concrete Model. FraMCos-6*; International Association of Fracture Mechanics for Concrete and Concrete Structures: Catania, Italy, 2007.
17. Polanco-Loria, M.; Hopperstad, O.S.; Børvik, T.; Berstad, T. Numerical predictions of ballistic limits for concrete slabs using a modified version of the HJC concrete model. *Int. J. Impact Eng.* **2008**, *35*, 290–303. [CrossRef]
18. Xiong, Y.B.; Hu, Y.L.; Xu, J.; Chen, J.J. Determining failure surface parameters of the Johnson-Holmquist concrete constitutive model. *Acta Armamentarii.* **2010**, *31*, 746–751. (In Chinese)
19. Xiong, Y.; Chen, J.; Hu, Y.; Wang, W. Study on the key parameters of the Johnson-Holmquist constitutive model for concrete. *Eng. Mech.* **2012**, *29*, 121–127. (In Chinese)
20. Zhang, R.-Q.; Ding, Y.-Q.; Tang, W.-H. The Failure Strength Parameters of HJC and RHT Concrete Constitutive Models. *Chin. J. High Press. Phys.* **2011**, *25*, 15–22. (In Chinese)
21. Fang, Q.; Kong, X.; Wu, H.; Gong, Z. Determination of Holmquist-Johnson-Cook Constitutive Model Parameters of Rock. *Eng. Mech.* **2014**, *31*, 197–204. (In Chinese)
22. Sun, Q.; Li, R.; Zhao, Y.; Sun, Y. Investigation on parameters of HJC model applied to Simulate perforation experiments of reinforced concrete. *Eng. Mech.* **2016**, *33*, 248–256. (In Chinese)
23. Su, W.L.; Li, X.G.; Xu, Y.; Jin, D.L. Numerical simulation of shield tool cutting concrete based on HJC model. *J. Zhejiang Univ. (Eng. Sci.)* **2020**, *54*, 1106–1114. (In Chinese)
24. Lei, W. Study on parameters of Holmquist-Johnson-Cook model for granite porphyry. *Chin. J. Comput. Mech.* **2016**, *33*, 725–731. (In Chinese)
25. Bi, C.C. Calibration of HJC constitutive parameters of Huashan granite and its blasting damage numerical simulation. Master's Thesis, Hefei University of Technology, Hefei, China, 2018. (In Chinese).
26. Lv, Y.; Lei, G. Numerical Simulation of Rock Fragmentation under PDC Cutter Assisted by Water Jet based on H-J-C Model. *Int. Core J. Eng.* **2021**, *7*, 18–27.
27. Lou, C.D.; Zhang, R.; Ren, L.; Zhou, J.F.; Peng, Y.; Zhang, Z.T. Determination and numerical simulation for HJC constitutive model parameters of Jinping marble. *IOP Conf. Ser. Earth Environ. Sci.* **2021**, *861*, 032074. [CrossRef]
28. Xie, B.; Yan, Z.; Du, Y.; Zhao, Z.; Zhang, X. Determination of Holmquist–Johnson–Cook Constitutive Parameters of Coal: Laboratory Study and Numerical Simulation. *Processes* **2019**, *7*, 386. [CrossRef]
29. Frenzel, C.; Käsling, H.; Thuro, K. Factors Influencing Disc Cutter Wear. *Geomech. Tunn.* **2008**, *1*, 55–60. [CrossRef]

30. Zhao, J.; Zhu, X.Y.; Hou, Z.; Liu, C.; Yang, S.; Xiao, X. Design and finite element analysis of a variable cross-section cutter ring. *Simul. Model. Pract. Th.* **2022**, *115*, 102423. [CrossRef]
31. Teale, R. The concept of specific energy in rock drilling. *Int. J. Rock Mech. Min. Sci. Geomech. Abstr.* **1965**, *2*, 57–73. [CrossRef]
32. Gertsch, R.; Gertsch, L.; Rostami, J. Disc cutting tests in Colorado Red Granite: Implications for TBM performance prediction. *Int. J. Rock Mech. Min.* **2007**, *44*, 238–246. [CrossRef]
33. Ning, B.; Xia, Y.; Lin, L.; Zhang, X.; He, Y.; Liu, Y. Experimental study on the adaptability of cutters with different blade widths under hard rock and extremely hard rock conditions. *Acta Geotech.* **2020**, *15*, 3283–3294. [CrossRef]
34. Cho, J.; Jeon, S.; Yu, S.; Chang, S. Optimum spacing of TBM disc cutters: A numerical simulation using the three-dimensional dynamic fracturing method. *Tunn. Undergr. Sp. Tech.* **2010**, *25*, 230–244. [CrossRef]
35. Li, X.H.; Du, W.; Huang, Z.L.; Fu, W.L. Simulation of Disc Cutter Loads Based on ANSYS/LS-DYNA. *Appl. Mech. Mater.* **2012**, *127*, 385–389. [CrossRef]
36. Zhang, A.N.; Zhu, Z.F.; Zhu, F. The Finite Element Simulation of Disc Cutter of Different Diameter Breaking Rock. *Adv. Mater. Res.* **2013**, *791–793*, 742–745. [CrossRef]
37. Choi, S.; Lee, S. Three-dimensional numerical analysis of the rock-cutting behavior of a disc cutter using particle flow code. *KSCE J. Civ. Eng.* **2015**, *19*, 1129–1138. [CrossRef]
38. Labra, C.; Rojek, J.; Oñate, E. Discrete/Finite Element Modelling of Rock Cutting with a TBM Disc Cutter. *Rock Mech. Rock Eng.* **2017**, *50*, 621–638. [CrossRef]
39. Zhou, X.; Zhai, S.; Bi, J. Two-Dimensional Numerical Simulation of Rock Fragmentation by TBM Cutting Tools in Mixed-Face Ground. *Int. J. Geomech.* **2018**, *18*, 6018004. [CrossRef]

Disclaimer/Publisher's Note: The statements, opinions and data contained in all publications are solely those of the individual author(s) and contributor(s) and not of MDPI and/or the editor(s). MDPI and/or the editor(s) disclaim responsibility for any injury to people or property resulting from any ideas, methods, instructions or products referred to in the content.